Journal of Sound and Vibration (2002) **249**(2), 371–397
doi:10.1006/jsvi.2001.3860, available online at http://www.idealibrary.com on IDEAL®

NON-LINEAR MODELLING OF HYDRAULIC MOUNTS: THEORY AND EXPERIMENT

A. Geisberger, A. Khajepour and F. Golnaraghi

Department of Mechanical Engineering, University of Waterloo, 200 University Avenue West, Waterloo, Ont., Canada N2L 3G1. E-mail: akhajepour@uwaterloo.ca

(*Received* 21 *September* 2000, *and in final form* 29 *June* 2001)

This paper focuses on the development of a complete non-linear model of a hydraulic engine mount and the evaluation of the model using a unique experimental apparatus. The model is capable of capturing both the low- and high-frequency behavior of hydraulic mounts. The results presented here provide a significant improvement over existing models by considering all non-linear aspects of a hydraulic engine mount. Enhancements to already published non-linear models include a continuous function that follows a simplistic yet effective approach to capture the switching effect and leakage through the decoupler, and upper chamber bulge damping. It is shown that the model developed here provides the appropriate system response over the full range of loading conditions (frequency and amplitude) encountered in practice. In order to obtain the parameter values for the non-linear model, a unique test apparatus is introduced. Using the experimental set-up, it is possible to verify the model of individual components of the mount, and later on test the behavior of the whole assembly. These data also establish the relative importance of several damping, inertia and stiffness terms. In addition, the measured responses of the mounts to loading at various frequencies and amplitudes are compared to the predictions of the mathematical model. The comparisons generally show a very good agreement (better than 10%), which corroborate the non-linear model of the mount. It is felt that this work will help engineers in reducing mount design time, by providing insight into the effects of various parameters within the mount.

1. INTRODUCTION

Vehicle occupants receive undesirable vibrations through one of two possible excitation sources. The first source, from engine eccentricity, typically contains frequencies in the range of 25–200 Hz with amplitudes generally less than 0·3 mm [1]. The second source of excitation originates from road inputs and engine torque during harsh accelerations. Road inconsistencies cause disturbances to the vehicle frame via the suspension system, whereas fierce accelerations cause excessive engine torque and motion at the mounts. Excitations of this nature are typically under 30 Hz and have amplitudes greater than 0·3 mm [1].

During low-frequency high-amplitude vibrations, the ideal mount should exhibit large stiffness and damping characteristics to reduce relative displacement transmissibility whereas for high-frequency low-amplitude vibrations the ideal mount should have low stiffness and damping characteristics. These conflicting properties indicate that an ideal mount system has stiffness and damping characteristics dependent on the amplitude of excitation. Hydraulic engine mounts have been developed to address the conflicting amplitude- and frequency-dependent characteristics desired for automotive applications.

The passive hydraulic mount, illustrated in Figure 1, has received attention in several publications. A thorough discussion on engine vibrations and the desired engine mount

0022-460X/02/020371 + 27 $35.00/0

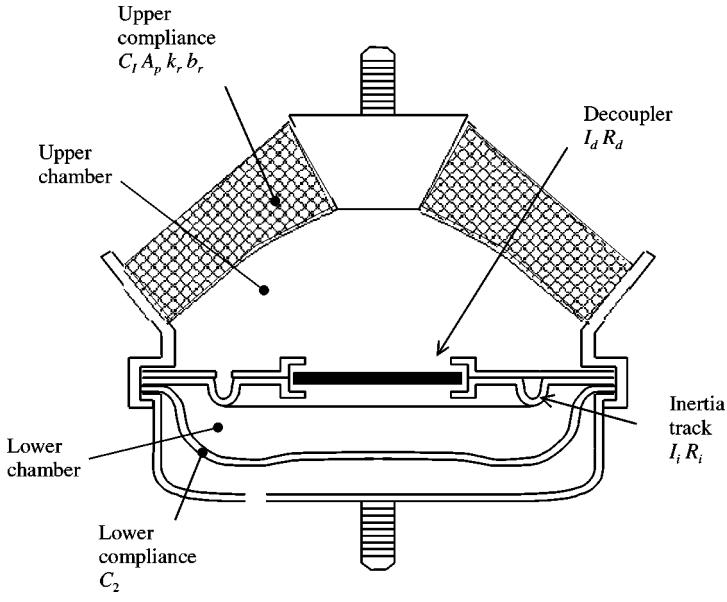

Figure 1. Cross-section of a typical hydraulic engine mount.

characteristics is provided by Brach and Haddow [1]. These authors also present a complete literature survey of models developed prior to the work by Singh *et al.* [2]. Since Singh *et al.* [2] have provided a complete description of the hydraulic mount operation and characteristics, there is no need to reconvey what has been stated already. The focus now turns to fluid mount models, primarily developed to accelerate hydraulic mount design.

Although Haddow has presented a complete account of earlier model development, the work by Flower [3] provides an excellent physical understanding of modelling techniques. The first paper by Singh *et al.* [2] develops linear time-invariant lumped parameter models for both free- and fixed-type decouplers. By splitting the hydraulic mount model into two, large-amplitude low-frequency and small-amplitude high-frequency, the decoupler non-linearity can be avoided. The authors also show that most prior models are special cases of their own and identify a problem with the hydraulic mount at high frequencies. Lee *et al.* [4] model the hydraulic engine mount using the bondgraph method, which is shown to be an efficient approach to developing the multi-disciplinary model equations.

More recent work begins to focus on the non-linear dynamics of hydraulic mounts. Kim and Singh begin an extensive non-linear analysis of hydraulic mounts. In reference [5], the non-linear properties are identified for a fluid mount with an inertia track. A non-linear lumped parameter model is formulated and compared with experimental data over time and frequency domains from 1 to 50 Hz. The content within their next two papers [6, 7] examines the dynamic characteristics of a hydraulic mount in an isolated case and within a simplified vehicle model. The non-linear lumped parameter model is updated to include decoupler switching characteristics and shown to be effective over the low-frequency 1–50 Hz range. Most of this work is culminated in reference [8]. In a theoretical and numerical study, Golnaraghi *et al.* [9] show that a simple non-linear model of a hydraulic mount can qualitatively describe the decoupler effect. The authors have also used perturbation techniques to investigate the behavior of the mount at resonance.

In reference [5], the non-linear properties are identified for a fluid mount with an inertia track. By experimentally measuring the chamber volumetric compliance, an equation is

fitted to the static curve, characterizing a non-linear chamber compliance. A non-linear form of the fluid resistance within the inertia track is also determined experimentally. A non-linear lumped parameter model is formulated and compared with experimental data over time and frequency domains from 1 to 50 Hz. Discrepancies between theory and experiment are attributed to gas–liquid phase transformation and cavitation phenomenon.

In this paper, we study and model the mount components individually and include all the involving non-linearities. We show that the mount assembled by the modelled components predicts the non-linear behavior of a hydraulic mount in both low and high frequencies. Modelling the decoupler contact with its cage allows us to include the mount geometry into the model and provides a means for design purposes. We introduce a unique experimental method whereby components of the hydraulic mount are isolated to enable parameter identification. We present the experimental design, parameter identification techniques, and measured versus model simulation results.

2. LUMPED PARAMETER LINEAR MODEL

Consider the hydraulic mount cross-section illustrated in Figure 1. The upper chamber compliance serves three main functions within the system. First, it contains the main structural stiffness and damping properties of the mount k_r and b_r respectively. The upper compliance also functions as a piston, with an effective pumping area A_p. Finally, the rubber structure adds volumetric compliance to the system, represented by C_1. The inertia track, a long column of fluid between chambers, is assigned lumped parameters I_i and R_i representing the inertia and resistance respectively. The other flow passage between the upper and lower chambers is through the decoupler. To begin constructing a system model, the decoupler is assigned linear lumped parameters I_d and R_d, which also represent an effective inertia and resistance. Assigning an effective inertia to the decoupler is the key to establishing high-frequency characteristics and has been included in references [3, 4, 10, 11]. Finally, the lower chamber contributes to the volumetric compliance and is modelled using a lumped parameter C_2.

Using the assigned parameters, the system schematic is converted to a lumped parameter model, illustrated in Figure 2. Variables within the system include the input excitation $X(t)$ and motion of the mount base $X_T(t)$. Also, the upper and lower chamber pressures are captured by $P_1(t)$ and $P_2(t)$ respectively. Flow through the inertia track $Q_i(t)$ and decoupler $Q_d(t)$ are highlighted in Figure 2, as well as the transmitted force to the mount base $F_T(t)$. Since the isolated test conditions use a fixed base, X_T is assumed to be zero in all equation developments.

The equations for the internal dynamics of the system shown in Figure 2 can be derived easily considering the continuity and momentum equations. The continuity equations are

$$C_1\dot{P}_1 = A_p\dot{X} - Q_i - Q_d, \qquad C_2\dot{P}_2 = Q_i + Q_d \tag{1, 2}$$

and the momentum equations become

$$P_1 - P_2 = I_i\dot{Q}_i + R_iQ_i, \qquad P_1 - P_2 = I_d\dot{Q}_d + R_dQ_d. \tag{3, 4}$$

The system of four state variables and one input, represents the internal dynamics of a fluid mount. Since the transmitted force is dependent on the decoupler position, two situations can be considered separately following the approach in references [6, 11]. When the

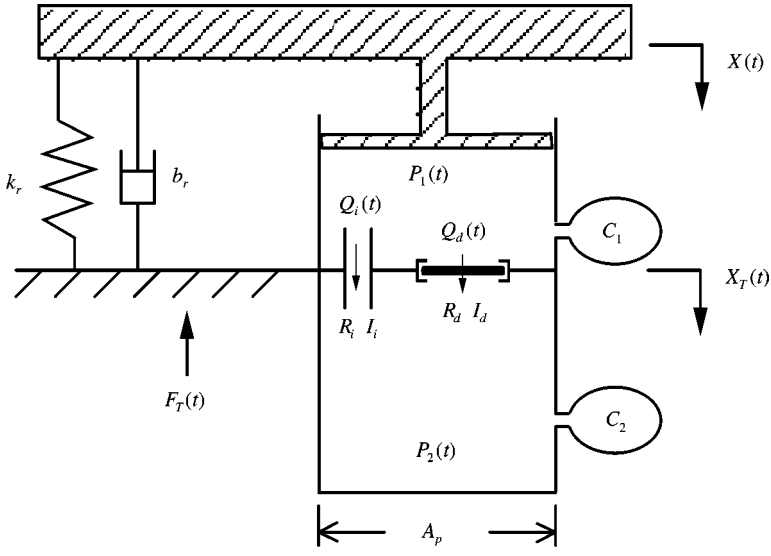

Figure 2. Lumped parameter system model.

decoupler is contacting the cage, the transmitted force equation is

$$F_T = k_r X + b_r \dot{X} + A_p(P_1 - P_2) + A_p P_2 \tag{5}$$

and where the decoupler is free, the equation becomes

$$F_T = k_r X + b_r \dot{X} + (A_p - A_d)(P_1 - P_2) + A_p P_2 + A_d R_d Q_d. \tag{6}$$

In both cases, the force transmitted to the mount base represents the sum of forces applied through the mechanical stiffness and damping parameters, along with the influence of internal chamber pressures. In equation (5), the upper chamber pressure acts on the mount base and piston area, while the lower chamber pressure is internal and does not influence F_T. In equation (6), the upper chamber pressure acts over the same area; however, it is now reduced by the decoupler hole. Also, the flow resistance through the decoupler influences the total transmitted force, captured initially with A_d, R_d, and Q_d respectively (similar to Colgate *et al.* [11]).

3. NON-LINEAR MODEL

The non-linear model evolves by enhancing the parameters of the linear model developed in the previous section. These enhancements capture non-linearities in the upper chamber stiffness, effective pumping area, chamber volumetric compliance, inertia track resistance, decoupler switching, transmitted force, and decoupler leak flow.

The model enhancements have been developed in conjunction with component evaluations, conducted experimentally and documented in reference [12] and presented later in this paper. To the best of the authors' knowledge, this section represents a new approach in non-linear modelling of hydraulic mounts and enhances the work of Kim and Singh [6, 7] and Colgate *et al.* [2].

3.1 UPPER CHAMBER

3.1.1. *Stiffness and damping*

In the linear modelling, the variables k_r and b_r have been introduced to represent the stiffness and damping properties within the upper chamber. In all papers reviewed, these variables are treated using the Voigt model for rubber, which assumes that both properties are invariant with frequency and amplitude. Here, the behavior of system parameters k_r and b_r in the frequency domain are shown to be dependent on the steady state amplitude and frequency of the excitation, as well as the preload force magnitude. Stiffness and damping are written in the non-linear form

$$k_r(w_{dr}, \tilde{X}, F_p), \qquad b_r(w_{dr}, \tilde{X}, F_p) \tag{7}$$

where w_{dr} represents a frequency of oscillation, $\tilde{X}$ the amplitude, and F_p is the preload force.

3.1.2. *Effective pumping area*

Under the static load of the engine mass, the rubber is deformed prior to the excitations. This preload force F_p yields a mean displacement of the rubber, which influences the effective pumping area. Effective pumping area is written as a function of preload force

$$A_p(F_p). \tag{8}$$

3.1.3. *Compliance*

Parameter C_1 represents the volumetric compliance of the upper chamber; however, it does not capture the damping that is evident in volumetric expansion. Colgate *et al.* [11] suggest that models will be moderately improved by including bulge damping effects; this work has captured the damping by including a resistance parameter on the flow into the compliant region. The continuity equation becomes

$$C_1\dot{P}_1 = Q_T + C_1R_1\dot{Q}_T. \tag{9}$$

Here, Q_T has been introduced to represent flow entering into the compliant region and the parameter R_1 represents the resistance to volumetric expansion. Variable P_1 is the same upper chamber pressure used in the linear model. The parameters C_1 and R_1, are dependent on the steady state volume amplitude $\tilde{V}_T$ and the frequency w_{dr} of excitations. Again, due to the geometrical changes under static preload, the non-linear parameters are also considered a function of preload force F_p:

$$C_1(w_{dr}, \tilde{V}_T, F_p), \qquad R_1(w_{dr}, \tilde{V}_T, F_p). \tag{10}$$

3.2 LOWER CHAMBER

In most designs, the main function of the lower chamber is to accommodate fluid transfer through the decoupler and inertia track. The volumetric compliance will have little influence on the system dynamics; here, a single volumetric compliance parameter C_2 is used to characterize the lower compliance. Depending on the design, it may be appropriate

to model the lower chamber compliance as a function of the static preload displacement, which is related to the preload force through the static load displacement curve:

$$C_2(F_p). \tag{11}$$

3.3. INERTIA TRACK

The linear inertia track model assumes a constant inertia I_i and resistance R_i. To enhance this model, some fluid dynamic properties are considered. Kim [8] has concluded that the fluid density can be considered constant and thermodynamic effects on flow are negligible for the oscillatory flow in an inertia track. However, Kim and Singh [6] have used an increased fluid inertia for laminar flow within the inertia track. All other papers regarding the inertia track dynamics assume a constant inertia parameter. From the experimental results [12], the inertia parameter is assumed constant in this work.

The resistance does not exhibit constant behavior. Since the inertia track flow is sinusoidal, the Reynolds number will change at each point within a period of flow oscillation changing flow resistance. In this work, the inertia track resistance R_i is separated into two non-linear parameters, R_i now represents the laminar resistance term while R_i' captures resistance in the turbulent region. The non-linear resistance equation becomes

$$\Delta P = (R_i + R_i'|Q_i|)\,Q_i. \tag{12}$$

The inertia term is now combined to provide a non-linear fluid momentum equation from equation (3):

$$P_1 - P_2 = I_i\dot{Q}_i + (R_i + R_i'|Q_i|)\,Q_i. \tag{13}$$

3.4. DECOUPLER

3.4.1. *Flow control*

When flow is oscillating across the decoupler orifice, the decoupler is considered open and the system behaves as a simple orifice. In equation (4), the decoupler is assigned a lumped inertia and resistance value similar to the inertia track. As with the inertia track, the decoupler inertia is assumed constant with amplitude and frequency of flow excitation; however, the free floating decoupler resistance is given non-linear parameters similar to equation (12). The non-linear momentum equation for the free floating decoupler becomes

$$P_1 - P_2 = I_d\dot{Q}_d + (R_d + R_d'|Q_d|)\,Q_d, \tag{14}$$

where the parameters R_d and R_d' represent the linear and non-linear resistance (due to turbulent flow) parameters respectively.

The addition of R_d' is not yet efficient to model the decoupler correctly. As the decoupler plate contacts its cage, all flow across the decoupler is blocked. To model this flow-stopping effect, we add a large flow resistance R_{add} to the momentum equation (14),

$$P_1 - P_2 = I_d\dot{Q}_d + (R_d + R_d'|Q_d| + R_{add})\,Q_d, \tag{15}$$

which is comparable to decreasing the orifice area. A similar approach has been taken by Kim and Singh [6, 7].

Using the volume of fluid and the flow direction across the decoupler as switching variables, a non-linear function for R_{add} is developed. The flow of fluid through the decoupler Q_d is integrated to obtain the decoupler volume V_d, with the decoupler initially positioned at the center at time zero. The decoupler position X_d is related to the volume by

$$X_d = V_d/A_d \tag{16}$$

As the decoupler contacts the cage limits, the resistance R_{add} is introduced to force $Q_d \to 0$. When the flow reverses direction, a result of the input pressure differential and momentum within the system, the additional resistance is removed as the decoupler travels relatively freely to the opposing cage limits. In references [7, 6], the decoupler switching characteristics are dependent on the volume of fluid passed through the decoupler and the pressure gradient between upper and lower chambers. However, this work has established that the switching characteristics are dependent on the volume of fluid and the direction of flow across the decoupler. During low-frequency excitations, this differentiation will have no influence on the non-linear response, since the low-inertia decoupler column moves in phase with the pressure gradient. at high frequencies, typically above 100 Hz, the inertia effect will cause the decoupler column to oscillate out of phase with the pressure gradient, thus making the pressure gradient independent of the flow direction. The switching characteristics in this paper have also been applied in the piecewise linear model of Colgate *et al.* [11]. A continuous function for the additional resistance function is

$$R_{add} = R_0 \mathrm{e}^{(X_d/X_0)\arctan(Q_d/Q_0)}, \tag{17}$$

where R_0 is a constant used to place the overall additional resistance magnitude in the appropriate range. The parameter X_0 is introduced to control the position at which the exponential increases, thus reflecting the decoupler cage height.

Flow-dependent characteristics of equation (17) are attained by switching the exponential sign using the principle branch of the arctangent function (arctan). The constant Q_0 is included to normalize the function and produce a crisp switching response. Figure 3(a) illustrates the decoupler sign convention and the desired function of R_{add}.

The final form of the momentum equation (14) becomes

$$P_1 - P_2 = I_d\dot{Q}_d + (R_d + R'_d|Q_d| + R_0 \mathrm{e}^{(X_d/X_0)\arctan(Q_d/Q_0)})\,Q_d. \tag{18}$$

3.4.2. *Transmitted force*

The transmitted force to the mount base is dependent on the decoupler position. When the decoupler is contacting the cage, the force equation is

$$F_T = k_r X + b_r\dot{X} + A_p(P_1 - P_2) + A_p P_2 \tag{19}$$

and when the decoupler is free, the force becomes

$$F_T = k_r X + b_r\dot{X} + (A_p - A_d)(P_1 - P_2) + A_p P_2 + A_d(R_d + R'_d|Q_d|)Q_d. \tag{20}$$

The term $A_d(R_d + R'_d|Q_d|)Q_d$ captures the force resulting from flow resistance through the free decoupler [11].

Two events occur to transform the transmitted force equations from equation (19) to equation (20). First, the decoupler closes and the pressure differential acts over the full area A_p, essentially $A_d \to 0$. Second, the flow across the decoupler becomes negligible, $Q_d \to 0$. Since Q_d is already controlled, only a decoupler area switching function is required.

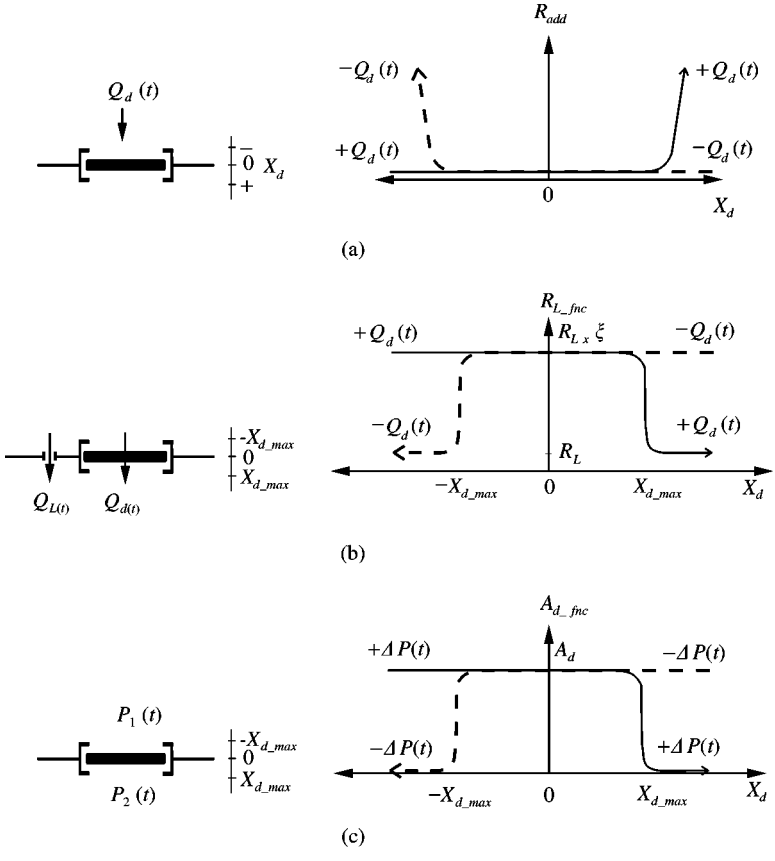

Figure 3. Non-linear decoupler developments: (a) additional resistance function; (b) leak flow function; and (c) area function for transmitted force.

In the transmitted force equation, the decoupler area is dependent on the decoupler position and pressure differential. These switching conditions are different from those used in the flow control, since the transmitted force is directly related to the pressure differential across, not flow through the decoupler.

The sign convention and non-linear area function A_{d_fnc} are illustrated in Figure 3(c). A continuous function for A_{d_fnc} using the arctangent function on both the pressure differential and decoupler displacement is developed. Constants P_0 and X_1 are introduced to normalize the function and control the switching function shape. The non-linear function becomes

$$A_{d\_fnc} = \frac{1}{\pi} A_d \left(\frac{\pi}{2} - \arctan\left(\frac{(2/\pi) X_d \arctan(\Delta P/P_0) - X_{d\_max}}{X_1} \right) \right) \tag{21}$$

and the complete non-linear transmitted force equation becomes

$$F_T = k_r X + b_r \dot{X} + (A_p - A_{d\_fnc})(P_1 - P_2) + A_p P_2 + A_d(R_d + R_d'|Q_d|) Q_d. \tag{22}$$

At this point, the non-linear analysis has captured the dominant switching characteristics of the decoupler, but an adjustment must be made in the cases where the decoupler does not completely block the flow.

3.4.3. *Leak flow*

The non-linear decoupler momentum equation completely stops the decoupler flow. However, some designs permit high-resistance flow through the closed decoupler, which is denoted by Q_L. The current decoupler model is enhanced to capture this leak flow with the addition of an orifice in parallel with the decoupler orifice, as illustrated in Figure 3(b).

It should be noted that the leak flow cannot be modelled as high-resistance flow through the decoupler. Since the decoupler flow is integrated to attain the position, it is important to preserve the memory of the decoupler plate by completely stopping the decoupler flow. A variable resistance orifice, which is open only when the decoupler is contacting the cage and the flow is in the appropriate direction, is developed. The resistance parameter R_L in Figure 3(b) represents the closed decoupler resistance, while R_{L_fnc} denotes the non-linear function. The parameter X_{d_max} is introduced to signify the maximum displacement accommodated by the decoupler, and ξ is used to raise the resistance to a relatively infinite value. The non-linear function becomes

$$R_{L\_fnc} = R_L + R_L\xi\left(1 - \frac{2}{\pi}\arctan\left(\frac{(2/\pi)(X_d)\arctan(Q_d/Q_o) - X_{d\_max}}{X_2}\right)\right), \tag{23}$$

where X_2 is introduced as a normalizing parameter that is used to control the non-linear function shape.

With the non-linear leak resistance function included, the equation for flow across the leak orifice becomes

$$P_1 - P_2 = R_{L\_fnc}|Q_L|Q_L. \tag{24}$$

Although not every decoupler design will exhibit some leak flow, this particular development will be used for the mount studied in reference [12].

4. NON-LINEAR MODEL FUNCTIONALITY

Of the non-linear developments, the decoupler switching is the most dominant. This section examines the model response to confirm functionality and considers the impact of the main non-linear decoupler parameter. Frequency domain characteristics are used to explain the decoupler operation over the complete range of excitations.

To attain frequency response characteristics from the non-linear model, the equations are simulated in the time domain by solving the set of simultaneous differential equations, then converted to the frequency domain. The solution method uses numerical differentiation and a new technique for stiff differential problems [13]. Using MATLAB, the set of equations are solved for a particular excitation condition and a Fourier transform is applied to the steady state response to achieve the frequency data at the maximum amplitude. For each excitation condition, the procedure is repeated to determine the complete frequency response curve.

4.1. LOW-FREQUENCY RESPONSE

The decoupler switching characteristics are investigated for low-frequency large-amplitude excitations by simulating the model with parameters in Table 1. For simplicity, the effect of turbulent flow resistance in the decoupler and inertia track is

TABLE 1

Non-linear model parameters

$k_r = 225$ N/mm	$R_i = 10{\cdot}5 \times 10^{-5}$ kg/s/mm^4
$b_r = 0{\cdot}1 \times 10^3$ kg/s	$R_i' = 0{\cdot}0$
$A_p = 2500$ mm^2	$I_i = 3{\cdot}8 \times 10^{-6}$ kg/mm^4
$A_d = 660$ mm^2	$R_d = 11{\cdot}7 \times 10^{-6}$ kg/s/mm^4
$C_1 = 3{\cdot}0 \times 10^4$ mm^5/N	$R_d' = 0{\cdot}0$
$C_2 = 2{\cdot}6 \times 10^6$ mm^5/N	$I_d = 7{\cdot}5 \times 10^{-8}$ kg/mm^4
$Q_0 = 1 \times 10^{-5}$ mm^3/s	$X_{d\_max} = 0{\cdot}53$ mm
$P_0 = 1 \times 10^{-5}$ N/mm^2	$X_0 = 0{\cdot}0315$ mm
$X_1 = 1 \times 10^{-6}$ mm	$R_L = 4{\cdot}15 \times 10^{-6}$ kg/mm^7
$X_2 = 1 \times 10^{-8}$ mm	$R_0 = 1 \times 10^{-16}$ kg/s/mm^4

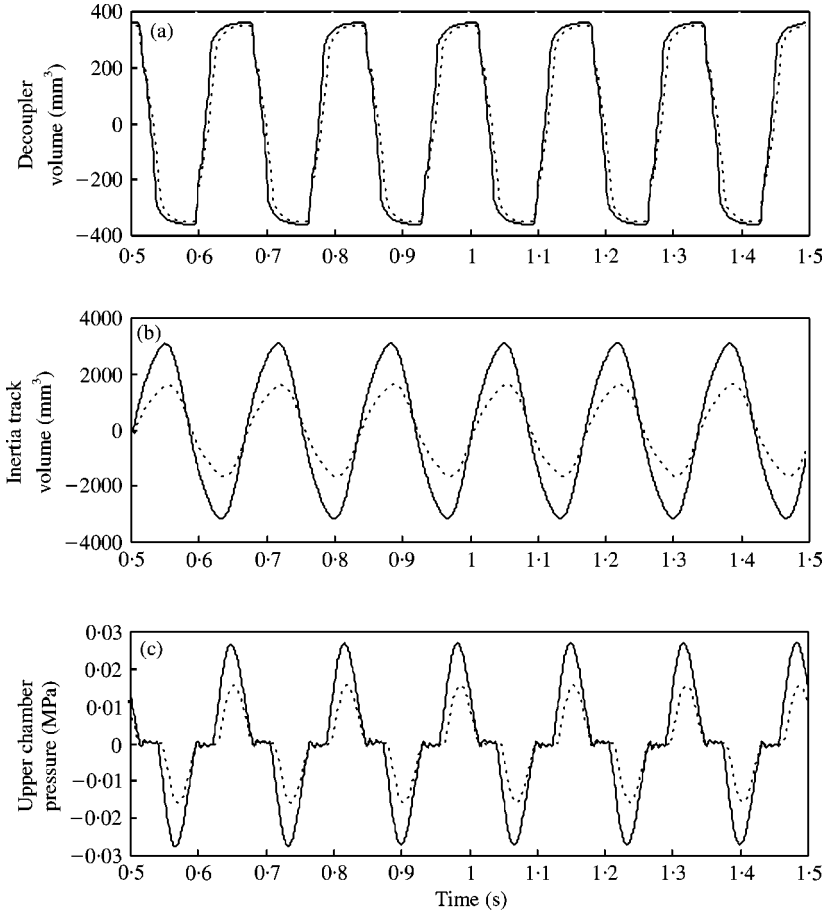

Figure 4. Time domain simulation of non-linear decoupler model (——, 2 mm P–P; ….,1 mm P–P): (a) decoupler volume; (b) inertia track volume; (c) upper-chamber pressure.

assumed to be negligible and as a result, both R_i' and R_d' are set to zero. Excitations having peak-to-peak amplitude levels of 1 and 2 mm are applied at 6 Hz to observe the decoupler volume, inertia track volume and upper chamber pressure. As Figure 4 indicates, the decoupler equations impose the desired non-linear mount characteristics. At approximately

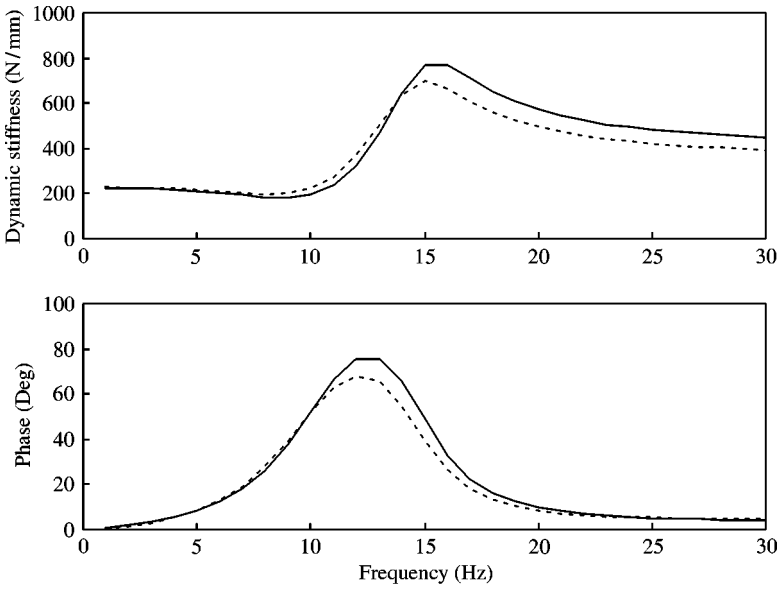

Figure 5. Low-frequency simulation of non-linear model (——, 2 mm P–P; ...., 1 mm P–P).

350 mm^3, the decoupler plate contacts the cage, stopping flow and pushing fluid through the inertia track, as illustrated in Figure 4(b). These time domain plots also indicate the amplitude sensitivity inherent in the model. As the excitation amplitude decreases, less fluid is pushed into the upper chamber which reduces decoupler cage contact time. Since the decoupler is free for a greater duration, the upper-chamber pressure and inertia track motion are both reduced. This characteristic is also observed in the frequency domain system response of Figure 5; dynamic stiffness is reduced after resonance due to the reduction in upper-chamber pressure.

4.2. HIGH-FREQUENCY RESPONSE

The same continuous non-linear model is now simulated with the parameters in Table 1 under high-frequency low-amplitude excitations as illustrated in Figure 6. For an excitation amplitude of 0·05 mm, the non-linear decoupler model demonstrates characteristics corresponding to a linear model. Excitation levels of 0·1 and 0·2 mm also demonstrate the amplitude-sensitive characteristics in the high-frequency range. With increased excitation amplitude, the decoupler fluid column motion enters the non-linear region around resonance as shown in Figure 7. Since the decoupler accommodates approximately 300 mm^3, the volume of fluid displaced into the upper chamber is limited and the peak upper-chamber pressure is diminished. These effects influence the system characteristics by reducing the peak dynamic stiffness and phase angle.

The frequency response characteristics in Figures 6 and 7 introduce an interesting phenomenon. Since the new hydraulic mount model is now a continuous non-linear set of differential equations, the non-linear frequency response is multi-valued. The resulting steady state solution now has more than one possible value for a given excitation condition. This system response is not only dependent on the amplitude and frequency of excitation, but also on the initial conditions. As cited in reference [14], a unique characteristic of

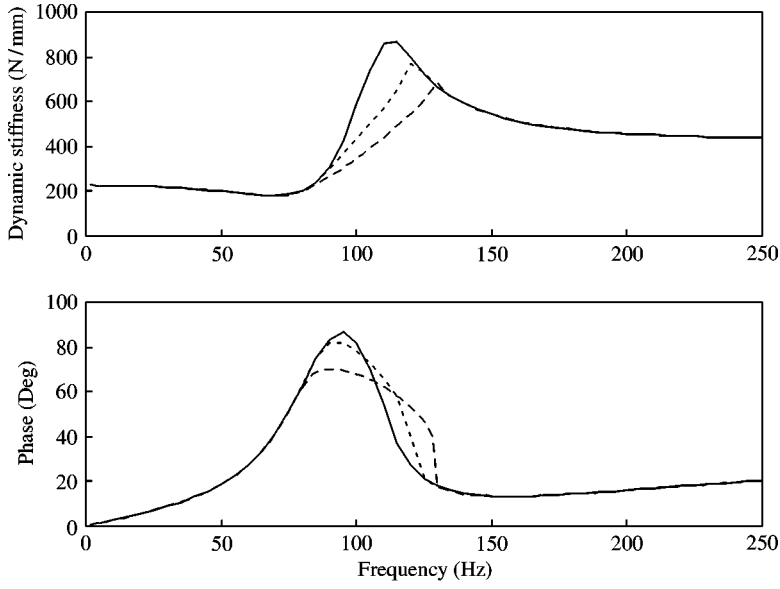

Figure 6. Dynamic stiffness characteristics of the non-linear model under high-frequency excitations (——, 0·05 mm P–P; ...., 0·75 mm P–P, ...,0·1 mm P–P).

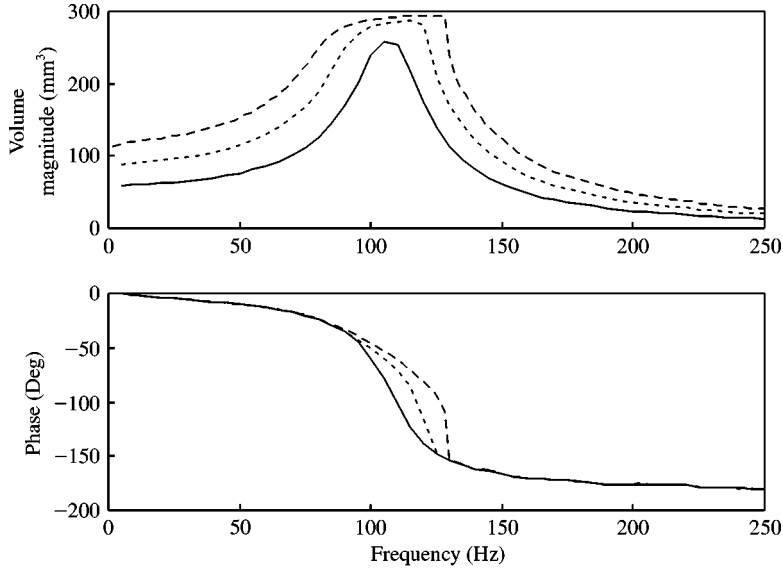

Figure 7. Decoupler motion in the non-linear model under high-frequency excitations (——, 0·05 mm P–P; ....,0·75 mm P–P; - - -,0·1 mm P–P).

non-linear systems is a "bend" in the frequency response, produced by unstable regions. To demonstrate that this unstable region exists within the non-linear decoupler model, frequency response curves have been calculated by sweeping the excitations. Using this technique, the initial conditions for a particular frequency become the last conditions of the previous steady state response. The impact of the initial conditions can be illustrated by

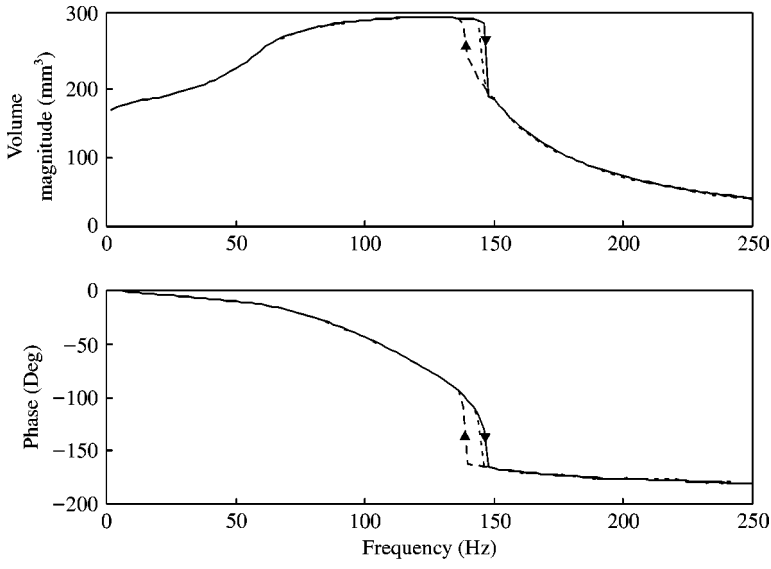

Figure 8. Decoupler motion indicating region on instability and dependence on sine sweep conditions (——, forward sweep; ....,mean dwell; ---, backward sweep).

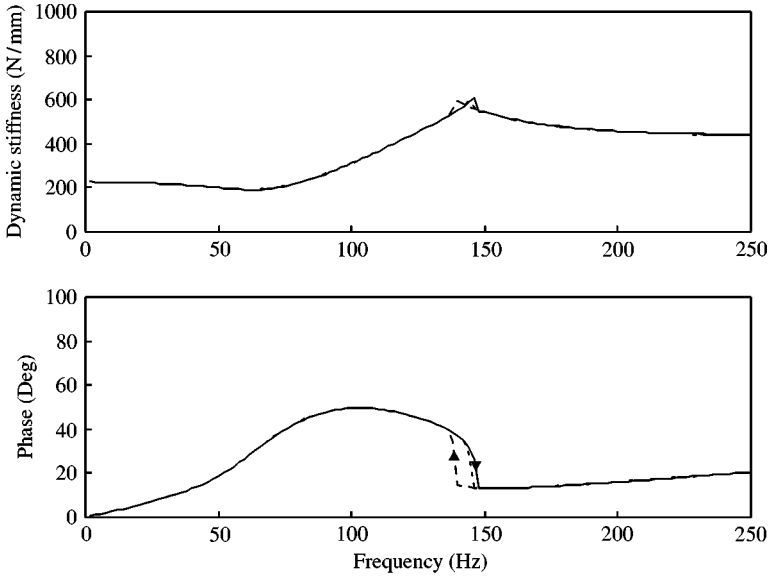

Figure 9. Dynamic stiffness and phase indicating the impact of sine sweep conditions (——, forward sweep; ...., mean dwell; ---, backward sweep).

comparing the frequency response for forward swept excitations and backward swept excitations.

Figure 8 shows how the amplitude and phase of the decoupler motion are dependent on excitation sweep direction, furthermore, the unstable region becomes evident. However, the impact of this phenomenon is somewhat diluted in the system dynamic characteristics. As Figure 9 illustrates, the dynamic stiffness is not greatly influenced by initial conditions; however, the phase does show a small region of instability.

To compare this simulation approach with the technique used for experimental evaluation, both Figures 9 and 8 also include the frequency response obtained using a mean dwell method. This method brings the system to rest for a period between excitations, to allow all internal dynamics to settle and resetting all initial conditions to zero. From the results, it is concluded that an acceptable frequency response is obtained by setting the initial conditions to zero for each excitation condition. Since the mount testing procedure also uses a mean dwell sine sweep process, the simulations with this technique will be used for model evaluation.

4.3. INFLUENCE OF NON-LINEAR DECOUPLER PARAMETERS

The switching characteristics of the non-linear decoupler model are controlled with the parameter X_0. This parameter limits the fluid volume through the decoupler via equation (18), reflecting the decoupler cage height. To verify the perceived impact of the decoupler parameter X_0 on the system response, the model is simulated with an excitation of 6 Hz and 2 mm P–P. Using the parameters in Table 1, the time domain decoupler volume V_d is plotted in Figure 10. Simulation results verify a direct relation between X_0 and the volume of fluid passing through the decoupler. Increasing the decoupler parameter limits the volume of fluid through the decoupler, indicative of a decreased cage height. Details of the parameter-to-geometry relations for hydraulic mounts are under investigation and will be presented in future.

5. EXPERIMENTAL DESIGN

The experimental apparatus in Figure 11 uses a hydraulic cylinder ①, driven via the servo-controlled actuator. With the base of the cylinder clamped to the machine base, linear motion of the actuator displaces fluid into a two-chamber vessel. Displacement control on the actuator becomes volume control by multiplying the fixed piston area by the linear actuator motion. While keeping the piston top open to atmosphere, actuator motion pushes fluid through a $\frac{1}{2}$-in diameter union joint ② into the identification vessel ③. The $5\frac{1}{2}$-in inside diameter vessel is constructed with $\frac{1}{2}$-in thick cast acrylic, contained between aluminum connectors. The modular design uses holding plates ④, clamped between vessel sections, to fix the various components in line with the controlled flow. High-frequency–pressure sensors ⑤ are used to collect output data on each side of the holding plate, capturing the pressure differential.

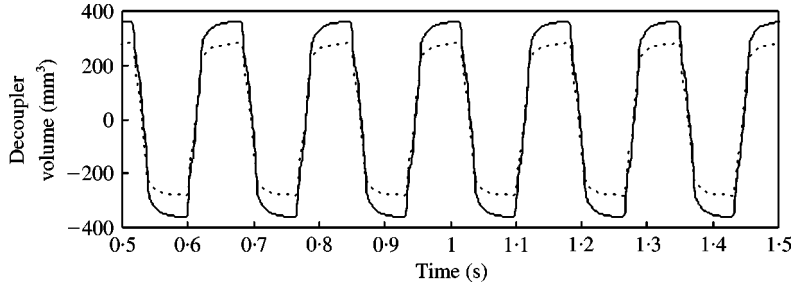

Figure 10. Simulation of decoupler volume indicating the response to changes in the decoupler parameter (——, X_0; ...., $X_0 + 30\%$).

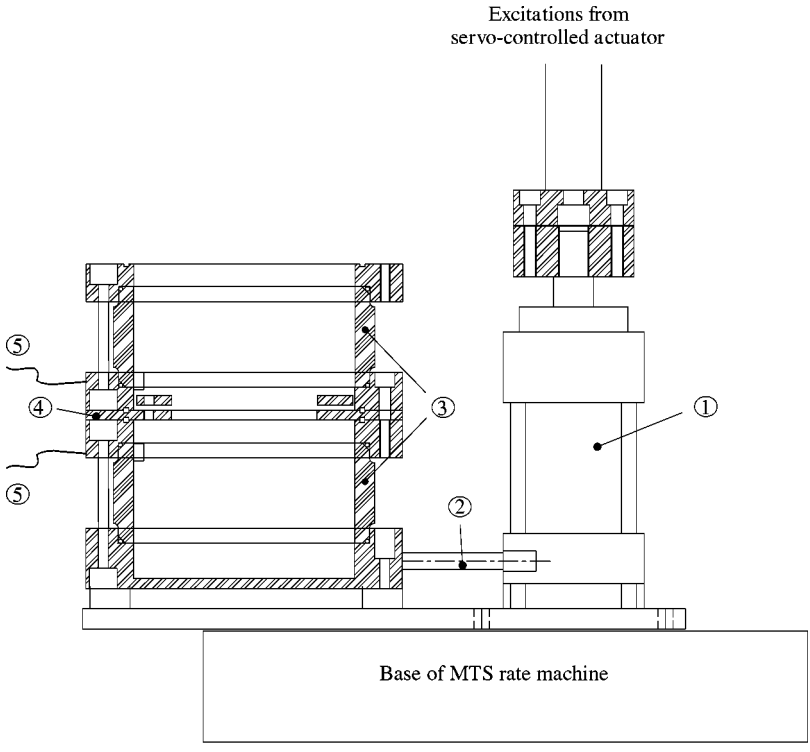

Figure 11. Schematic of experimental test apparatus.

6. PARAMETER IDENTIFICATION

6.1. UPPER CHAMBER

As discussed in section 3.1, the non-linear stiffness k_r and damping b_r parameters are defined to be a function of excitation amplitude $\tilde{X}$, driving frequency w_{dr}, and preload force F_p. Since these parameters are only dependent on the conditions applied to the whole mount system, the internal fluid system dynamics have no influence on the stiffness and damping parameters. The approach to investigating these parameters is to remove the fluid from the hydraulic mount and conduct tests on the upper compliance, effectively in isolation.

The non-linear model for the effective pumping area $A_p(F_p)$ is dependent on the preload force. As the mount is displaced under the preload force, the rubber deforms so that the effective piston area changes. To investigate this relationship, the experimental apparatus with the configuration shown in Figure 12 was used to isolate the upper compliance. By completely filling the vessel with fluid below the compliance, ensuring no air pockets are present, the changes in displacement at the mount top pushed fluid into the lower vessel chamber. Using pressure sensor feedback, the vessel pressure was maintained at 5 psi. As the mount was displaced in increments of 1 mm, the pressure control repositioned the actuator to accommodate the fluid displaced. Measurements of mount displacement and actuator position were tabulated and used to determine the effective area as a function of mount displacement as shown in Figure 13.

Once the stiffness, damping and effective pumping area parameters are established, the volumetric compliance parameters can be investigated. Using the test configuration

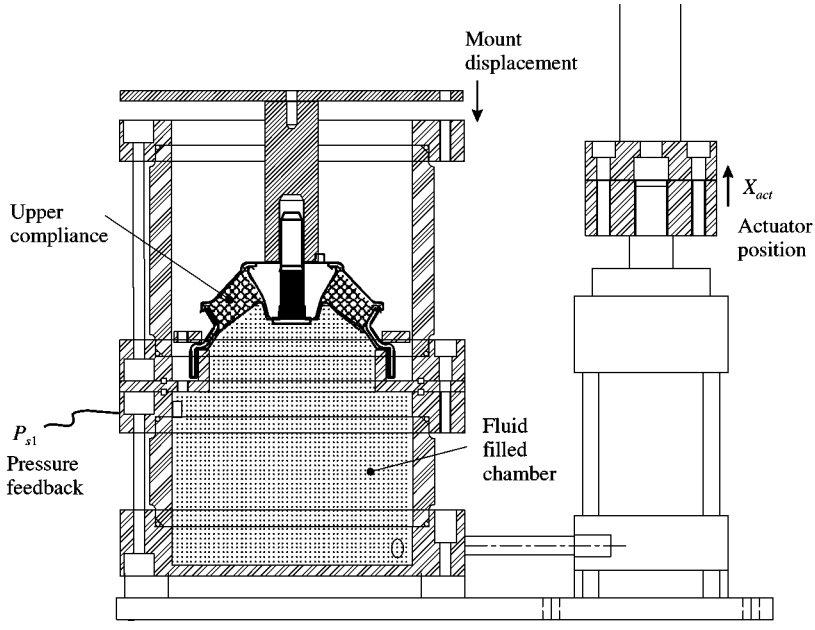

Figure 12. Test configuration for measuring the effective area and volumetric compliance parameters.

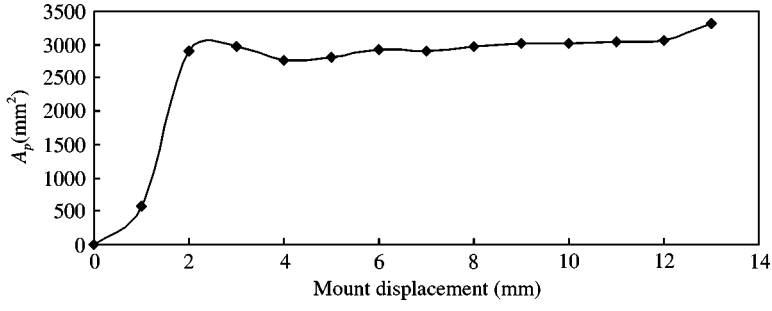

Figure 13. Plot of effective pumping area versus mount displacement (solid points indicate measured data).

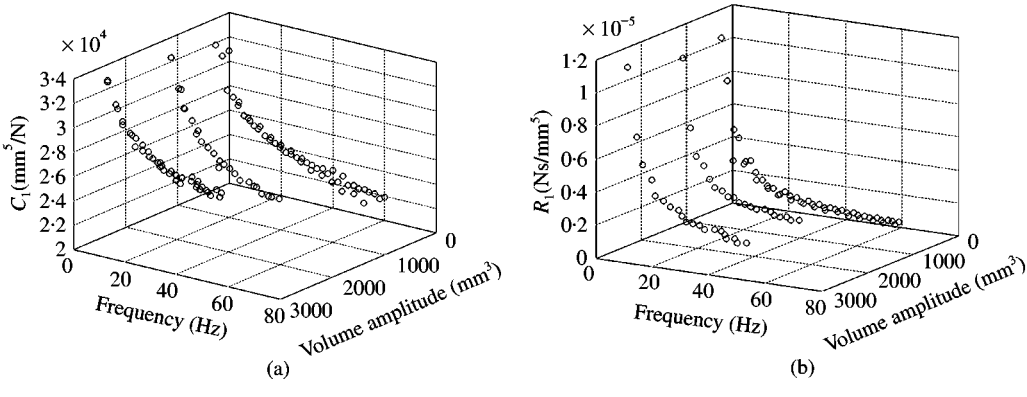

Figure 14. Upper compliance parameters identified at 15 psi mean pressure using the test apparatus: (a) volumetric compliance; (b) bulge damping.

illustrated in Figure 12, the upper compliance is displaced by the amount corresponding to the 1700 N preload. A known volume of fluid is then forced into the upper chamber and pressure readings are collected. Previous experimental studies documented by Kim and Singh [5] limit the investigation of compliance to static analysis; however, in this work dynamic characteristics of the volumetric compliance and bulge damping parameters, $C_1(w_{dr}, \tilde{V}_T, F_p)$ and $R_1(w_{dr}, \tilde{V}_T, F_p)$ are investigated by establishing a local linear response for various driving frequencies w_{dr} and volume amplitudes $\tilde{V}_T$. This is achieved by applying sinusoidal actuator excitations and measuring lower-chamber pressure response. The excitations are applied under a controlled mean pressure of 15 psi, and steady state time domain data is acquired for actuator position X_{act} and pressure P_{s1}. The actual volume of fluid passing into the upper chamber V_{actual} is then computed and the parameters C_1 and R_1 are identified and shown in Figure 14.

7. LOWER-CHAMBER COMPLIANCE

The mount under investigation is considered to be a single-load-bearing-chamber (SLBC) mount, since the lower chamber serves mainly as a fluid transfer area [15]. Essentially, the lower-chamber compliance acts as a diaphragm, contributing little to the volumetric stiffness of the system. However, the assignment of a compliance parameter, $C_2(F_p)$, to the lower-chamber is still carried out. This parameter is only dependent on the preload force, or the mean volume of fluid in the lower chamber.

To isolate the C_2 parameter, the test apparatus was used with the lower chamber fastened across the holding plate as illustrated in Figure 15. The static volume versus pressure curve was measured and is plotted in Figure 16.

During model simulation, the C_2 parameter is calculated by first estimating the volume of fluid displaced into the lower chamber under the preload force. This is done using the effective pumping area curve in Figure 13. The slope of Figure 16 at this volume level is used to approximate the volumetric compliance of the lower chamber.

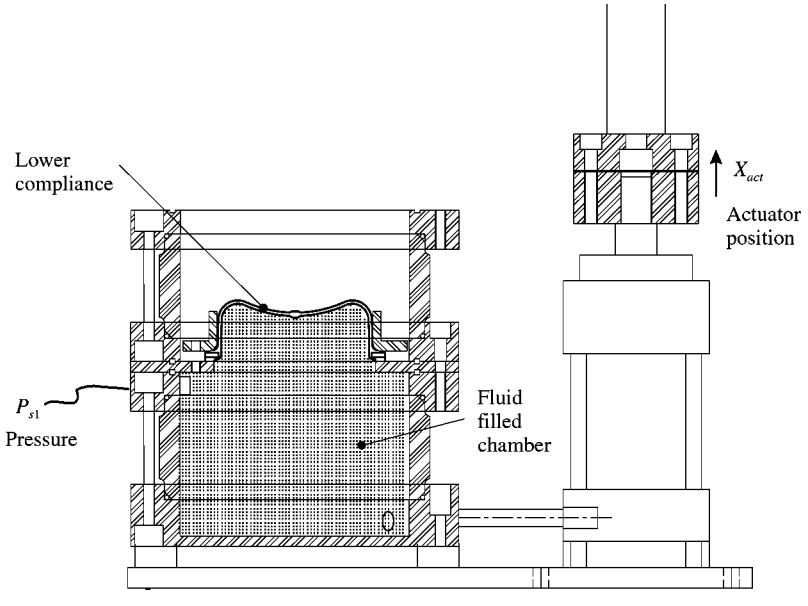

Figure 15. Test configuration for determining the volumetric compliance of the lower chamber.

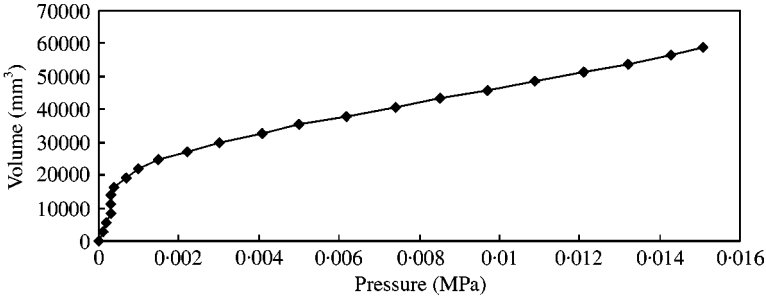

Figure 16. Static measurements of lower-chamber volumetric expansion versus pressure (solid points indicate measured data).

8. INERTIA TRACK PARAMETERS

Inertia track parameters are identified experimentally using the test apparatus configuration shown in Figure 17. The decoupler and inertia track assembly is bolted to the holding plate within the identification vessel. By blocking the decoupler, the fluid flow across the holding plate becomes the inertia track flow and transducer measurements P_{s1} and P_{s2} form the pressure differential in the momentum equation.

The parameters I_i, R_{i1} and R_{i2} (see section 3.3) are first investigated using frequency sweep data and a simplified linear momentum equation. Sinusoidal excitations are applied to the actuator and steady state time domain data are acquired for the actuator position X_{act} and both chamber pressures P_{s1} and P_{s2}. To introduce this method, the inertia track momentum equation is written in terms of the measured experimental variables,

$$\Delta P_{s1-s2} = I_i \dot{Q}_{actual} + (R_i + R_i' |Q_{actual}|) Q_{actual}, \tag{25}$$

where Q_{actual} represents the time derivative of V_{actual} which is calculated from the flow sent by ① in Figure 11 to the experimental apparatus. For each time sample of pressure differential and flow, equation (25) defines the relationship between variables within the isolated system. In theory, this suggests that three samples of measured data are enough to set up three equations and solve each of the desired parameters. If a sequence of time domain data is acquired, the least-squares method will determine the best estimate of system parameters. This approach first requires that the sequence of measurements be placed in matrix form, as follows:

$$\begin{bmatrix} {}^1\Delta P_{s1-s2} \\ {}^2\Delta P_{s1-s2} \\ \vdots \\ {}^n\Delta P_{s1-s2} \end{bmatrix} = \begin{bmatrix} {}^1\dot{Q}_{actual} & {}^1Q_{actual} & {}^1|Q_{actual}|Q_{actual} \\ {}^2\dot{Q}_{actual} & {}^2Q_{actual} & {}^2|Q_{actual}|Q_{actual} \\ \vdots & \vdots & \vdots \\ {}^n\dot{Q}_{actual} & {}^nQ_{actual} & {}^n|Q_{actual}|Q_{actual} \end{bmatrix} \begin{bmatrix} I_i \\ R_{i1} \\ R_{i2} \end{bmatrix}. \tag{26}$$

By assigning each matrix to the notation,

$$Y = \begin{bmatrix} {}^1\Delta P_{s1-s2} \\ {}^2\Delta P_{s1-s2} \\ \vdots \\ {}^n\Delta P_{s1-s2} \end{bmatrix}, \quad U = \begin{bmatrix} {}^1\dot{Q}_{actual} & {}^1Q_{actual} & {}^1|Q_{actual}|Q_{actual} \\ {}^2\dot{Q}_{actual} & {}^2Q_{actual} & {}^2|Q_{actual}|Q_{actual} \\ \vdots & \vdots & \vdots \\ {}^n\dot{Q}_{actual} & {}^nQ_{actual} & {}^n|Q_{actual}|Q_{actual} \end{bmatrix}, \quad \beta = \begin{bmatrix} I_i \\ R_{i1} \\ R_{i2} \end{bmatrix},$$

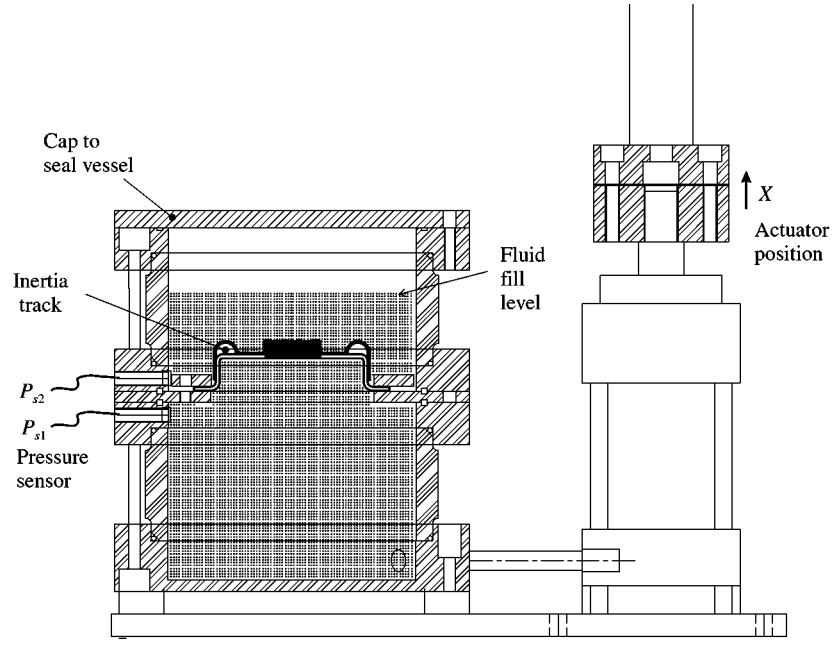

Figure 17. Test configuration for isolating the inertia track parameters.

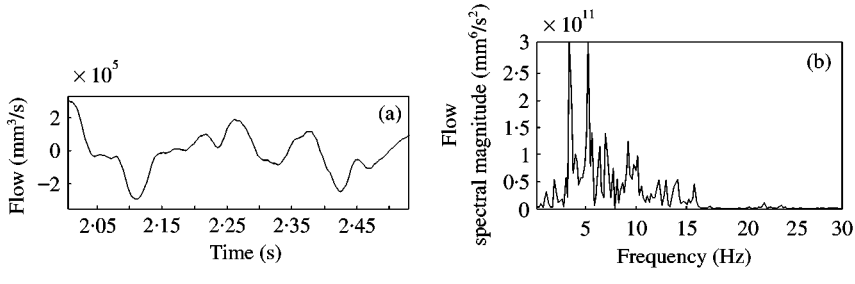

Figure 18. Isolated inertia track excitation plots including: (a) time domain segment of random flow input; (b) power spectral density of complete flow perturbation.

the least-squares parameter estimation is then applied using

$$\beta^* = (U^{\mathrm{T}}U)^{-1}U^{\mathrm{T}}Y, \tag{27}$$

where β^* is the least-squares estimate of the parameters in β (see references [16, 17]).

To apply this technique, a random perturbation is applied to the actual volume input as illustrated in Figure 18(a). The frequency spectrum of the excitation is measured and plotted in Figure 18(b), which indicates whether the perturbation is within the frequency range of interest. The random excitation is applied for 10 s and sampled every 0·002 s. Data samples are assembled into the form presented in equation (26) to obtain the inertia track parameters and the estimated output is illustrated in Figure 19. Parameter estimation using this technique identifies $I_i = 3{\cdot}38 \times 10^{-6}$ kg/mm^4, $R_i = 6{\cdot}52 \times 10^{-5}$ kg/s mm^4, and $R_i' = 4{\cdot}49 \times 10^{-13}$ kg/mm^7.

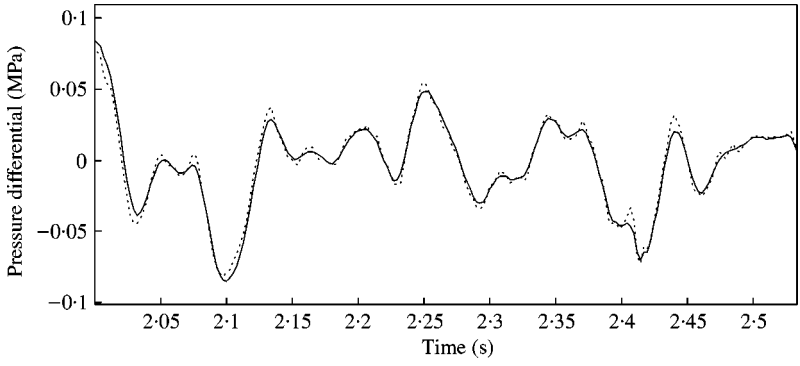

Figure 19. Time domain segment of measured pressure differential versus model output using estimated parameters (——, measured; ...., Least square estimate).

9. DECOUPLER PARAMETERS

The experimental test configuration used to identify the decoupler parameters is shown in Figure 20. To ensure that all flow forced across the holding plate passes through the decoupler, the inertia track is blocked. The non-linear decoupler model established in section 3.4 includes a non-linear momentum equation in parallel with a variable resistance orifice for the decoupler leak,

$$P_1 - P_2 = I_d\dot{Q}_d + (R_d + R'_d|Q_d| + R_0 e^{(X_d/X_0)\arctan(Q_d/Q_0)})\, Q_d, \tag{28}$$

$$P_1 - P_2 = R_{L\_fnc}|Q_L|\, Q_L \tag{29}$$

respectively. Five parameters in equations (28) and (29) control the complete behavior of the non-linear decoupler model. The inertia I_d and resistances R_d and R'_d govern the decoupler properties when operating in the uncoupled region, while X_0 controls the decoupler switching. Also, the non-linear leak flow resistance R_{L_fnc}, exists as R_L when the decoupler is closed and is controlled with the parameter X_{d_max}. Even with the system experimentally isolated, equations (28) and (29) represent a complex five-parameter identification task with one state variable X_d. As a consequence, the following approach utilizes a two-step identification procedure.

The first experimental test is a frequency sweep of volume excitation that prevents the decoupler from contacting its cage. The mathematical model will then follow the form

$$P_1 - P_2 = I_d\dot{Q}_d + (R_{d1} + R_{d2}|Q_d|)Q_d,$$

which is a reduced form of equation (28). A reasonable approximation for parameters R_d and R'_d is established using the intersection and slope of the linear trendline of the frequency response. Identified parameters are plotted over the decoupler flow amplitude in Figure 21.

The isolated response demonstrates that the decoupler inertia remains constant across various flow conditions, while the resistance increases with the decoupler flow. For the mount under investigation, the parameters are found to be $I_d = 8{\cdot}28 \times 10^{-8}$ kg/mm^4, $R_d = 4{\cdot}58 \times 10^{-6}$ kg/s mm^4, and $R'_d = 4{\cdot}25 \times 10^{-11}$ kg/mm^7.

The two remaining parameters X_0 and R_L combine with the decoupler state X_d, to form a state and parameter identification problem. Since the switching characteristics under

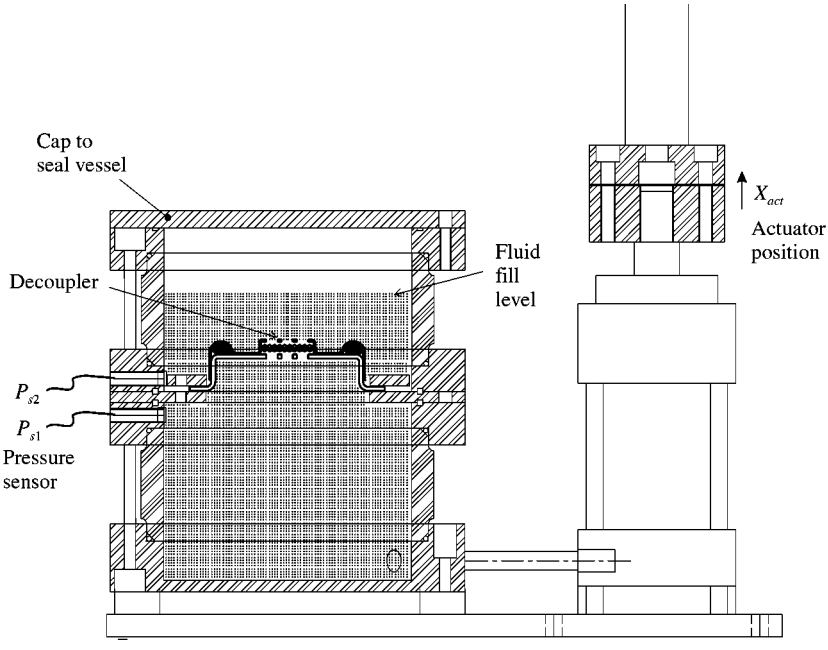

Figure 20. Test configuration for isolating the decoupler parameters.

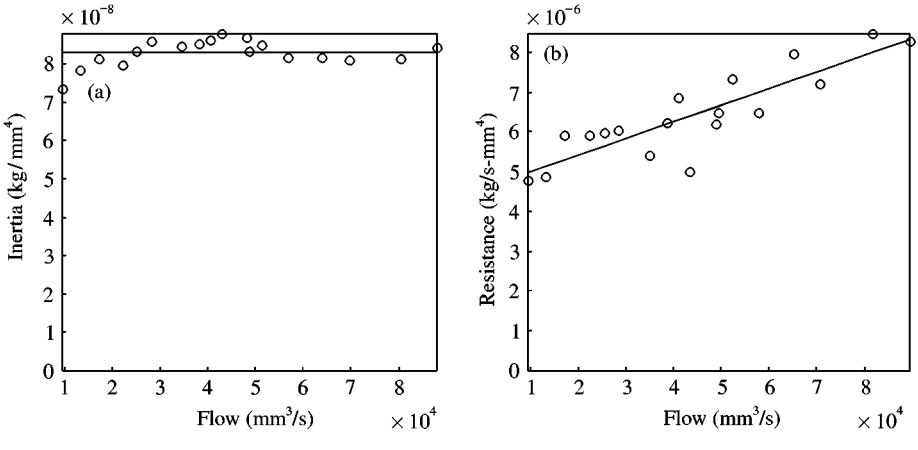

Figure 21. Parameter trends with respect to decoupler flow, for: (a) fluid column inertia; (b) resistance.

investigation are independent of excitation frequency, the second isolated test is conducted by applying low-frequency random perturbations. Under these excitations the decoupler inertia has negligible impact on the isolated system response; therefore, it is removed from equations (28) and (29). Also, the non-linear leak flow resistance function R_{L_fnc} is reduced to the R_L parameter, since the flow is controlled when isolated in the test apparatus. The isolated switching model becomes

$$\Delta P_{s1-s2} = (R_d + R'_d|Q_d| + R_0 \mathrm{e}^{(X_d/X_0)\arctan(Q_d/Q_0)})\, Q_d, \tag{30}$$

$$\Delta P_{s1-s2} = R_L|Q_L|\, Q_L. \tag{31}$$

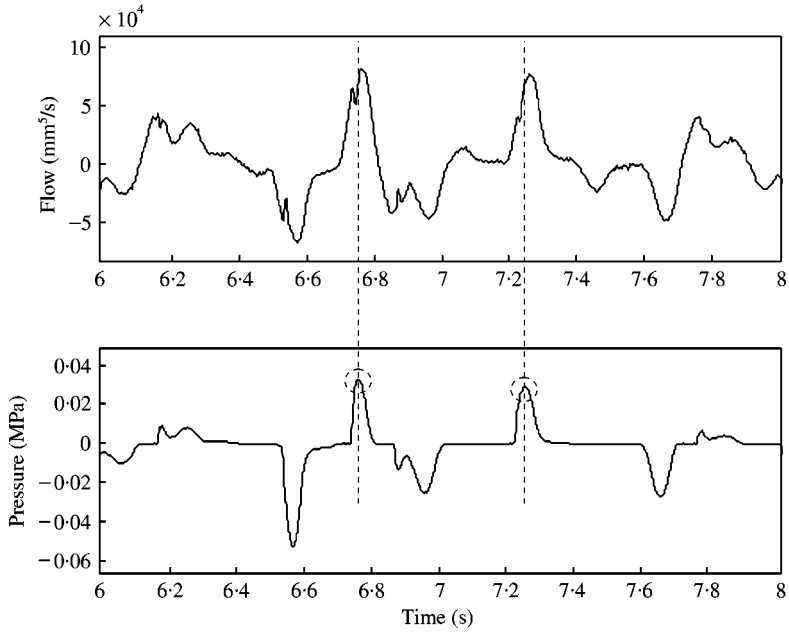

Figure 22. Time segment of the decoupler input flow and pressure differential, indicating locations where leak resistance is identified.

where Q_0 and R_0 are held at constant parameters 1×10^{-5} mm^3/s and 1×10^{-16} kg/s/mm^4 respectively. In equations (30) and (31), the actual flow controlled across the decoupler Q_{actual} now represents the total volume accommodated via the decoupler and leak flow,

$$Q_{actual} = Q_L + Q_d. \tag{32}$$

Also, the absolute value signs in equations (30) and (31) are resolved into algebraic equations by noting that the signs of Q_d and Q_L are equivalent to that of the input Q_{actual}.

The equation for Q_d, is simplified into a function of the state X_d, parameters X_0 and R_L, and input Q_{actual},

$$Q_d = f(X_d, X_0, R_L, Q_{actual}). \tag{33}$$

Using the decoupler flow (33) and equation (32), the system output equation is reduced to

$$\Delta P_{s1-s2} = g(X_d, X_0, R_L, Q_{actual}). \tag{34}$$

Equations (33) and (34) form the state and parameter identification problem, where the decoupler state has to be predicted and each parameter estimated, for each position in time. Convergence issues arise when attempting to predict X_d and identify X_0 and R_L all in one algorithm. , R_L is calculated prior to predicting the state variable.

The leak flow resistance is first calculated using the measured pressure differential output, as illustrated in Figure 22. The peak pressure differential measurements (circled locations in Figure 22) represent the high-resistance leak flow around the closed decoupler, occurring when $Q_L = Q_{actual}$. The R_L parameter is then calculated using

$$R_L = \frac{{}^*\Delta P_{s1-s2}}{{}^*Q^2_{actual}}, \tag{35}$$

where $^*\Delta P_{s1-s2}$ and $^*Q_{actual}$ represent the measured data at the pressure differential peaks.

Once leak resistance is estimated, the functions in equations (33) and (34) are reduced to just one unknown parameter X_0, and the state variable X_d:

$$Q_d = f(X_d, X_0, Q_{actual}), \qquad \Delta P_{s1-s2} = g(X_d, X_0, Q_{actual}). \tag{36, 37}$$

Equations (36) and (37) are discretized, using

$$Q_{d,k} = \frac{A_d(X_{d,k+1} - X_{d,k})}{T}, \tag{38}$$

where k represents the kth sample point of the data series, sampled at time intervals T. The parameter A_d is the decoupler surface area and is calculated from the geometry. Using equation (38) to transform equations (36) and (37) into discrete form gives

$$V_{d,k+1} = f(X_{d,k}, X_{0,k}, Q_{actual,k}, k), \qquad \Delta P_{s1-s2,k} = g(X_{d,k}, X_{0,k}, Q_{actual,k}, k). \tag{39, 40}$$

Identification of both states and parameters presents a unique problem. First, the state estimation problem formulation assumes knowledge of all system parameters. The system identification problem to determine parameters then assumes the availability of the variables or states within the system. To work around this problem, the parameter X_0 is written as a state variable and appended to the original state. Since X_0 is constant, the new state equation becomes

$$X_{0,k+1} = X_{0,k}, \tag{41}$$

this state is then added to $V_{d,k+1}$ to form the new state equation vector

$$\bar{X}_{k+1} = \begin{bmatrix} X_{d,k+1} \\ X_{0,k+1} \end{bmatrix} = \begin{bmatrix} f(X_{d,k}, X_{0,k}, Q_{actual,k}, k) \\ X_{0,k} \end{bmatrix} \tag{42}$$

and the state vector

$$\bar{X}_k = \begin{bmatrix} X_{d,k} \\ X_{0,k} \end{bmatrix}. \tag{43}$$

Therefore, the new isolated decoupler system becomes

$$\bar{X}_{k+1} = f(\bar{X}_k, Q_{actual,k}, k), \qquad \Delta P_{s1-s2,k} = g(\bar{X}_k, Q_{actual,k}, k). \tag{44, 45}$$

The new state vector (43) transforms the system into a non-linear state estimation problem, which is then solved using the extended Kalman filter:

$$\bar{X}_{k+1} = f(\bar{X}_k, U_k, k) + w_k, \qquad Z_k = g(\bar{X}_k, U_k, k) + q_k, \tag{46, 47}$$

where U_k and Z_k represent the system input and output respectively. w_k denotes disturbance noise on the states, while q_k represents measurement noise on the output. Extended Kalman filter algorithm is used to identify state variables from equations (46) and (47).

Random perturbations are applied to the isolated system for approximately 20 s and sampled at time intervals $T = 0{\cdot}004$ s. Input and output measurements are used to solve for

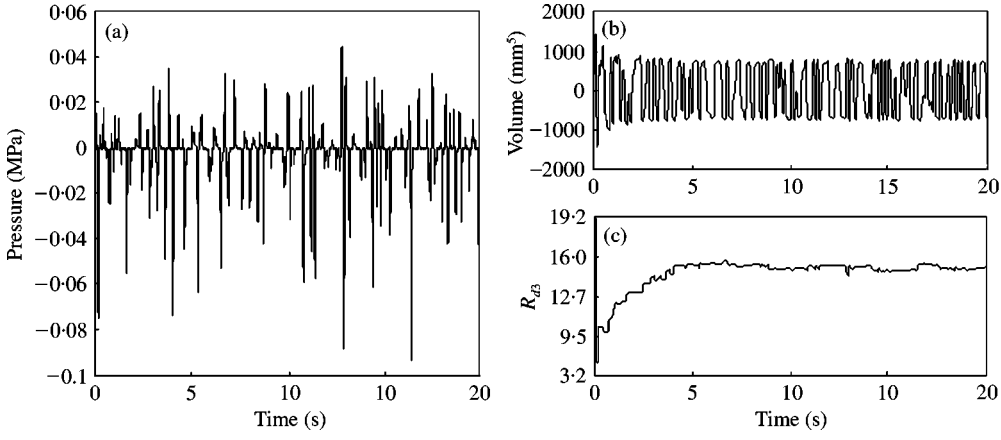

Figure 23. Decoupler state and parameter identification: (a) pressure differential across decoupler, (b) decoupler volume state variable, (c) decoupler switching parameter.

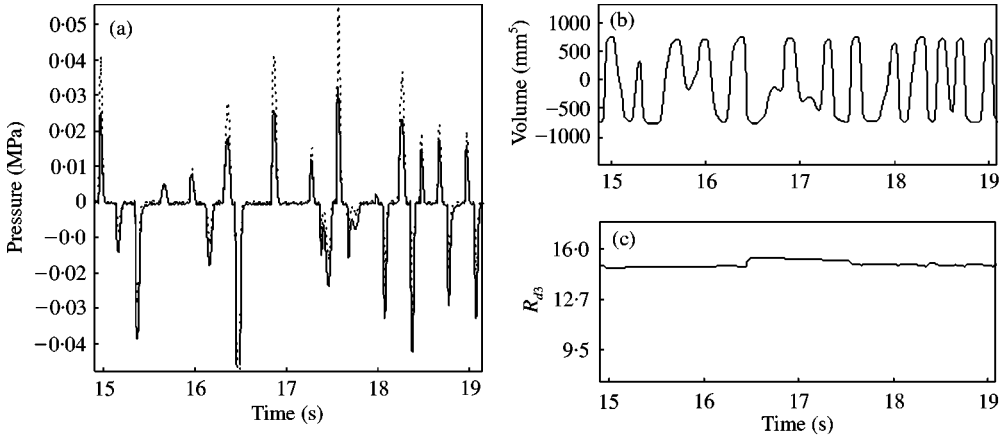

Figure 24. Close up of the decoupler state and parameter identification: (a) pressure differential across decoupler (——, measured; ...., Estimate), (b) decoupler volume state variable, (c) decoupler switching parameter.

R_L, then analyzed using the filter algorithm. The results in Figure 23 show how the procedure converges on parameter estimates, while Figure 24 provides a closer look at the predicted state motion and output accuracy. For the decoupler under investigation, this identification procedure obtained $R_L = 9{\cdot}21 \times 10^{-9}$ kg/mm^7, and $X_0 = 0{\cdot}07$ mm.

The X_{d_max} parameter, used as the switching parameter in the non-linear transmitted force and leak flow equations, is determined using the converged decoupler state estimate X_d. As Figure 24(b) indicates, the maximum volume through the decoupler is about 750 mm^3 where since the decoupler area is 660 mm^2, the estimated $X_{d\_max} = 1{\cdot}14$ mm.

10. MODELLED VERSUS MEASURED SYSTEM RESPONSE

Using the estimated parameters obtained so far and the model developed so far, the experimental and simulation results for the whole mount behavior is compared over the complete range of excitations. Figure 25 shows the low-frequency simulation and real

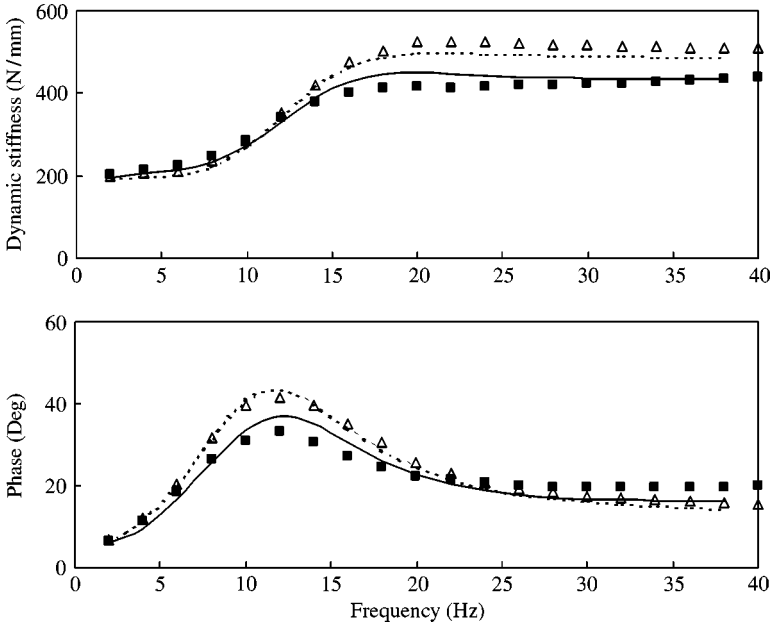

Figure 25. Low-frequency simulation versus measured response, on a mount including a decoupler and inertia track (■, 1 mm P–P, △, 2 mm P–P; ——, 1 mm P–P simulated.; 2 mm P–P simulated).

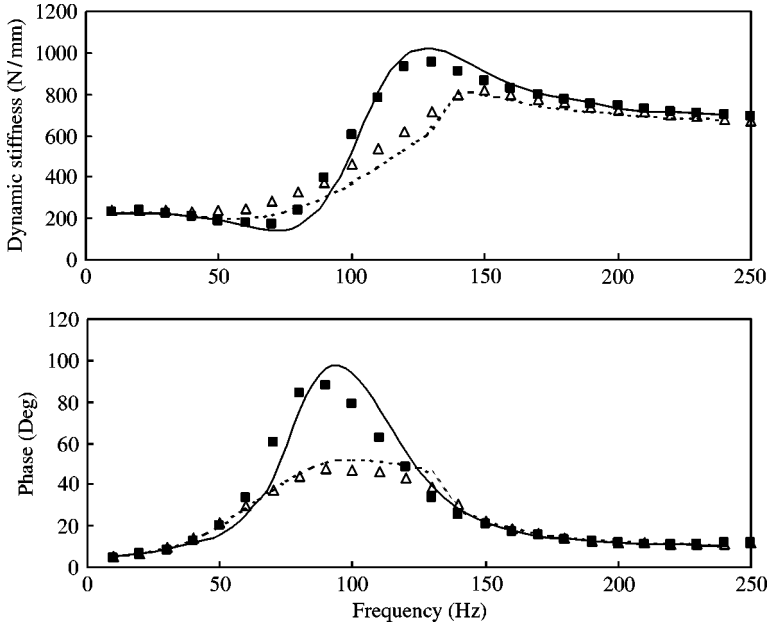

Figure 26. High-frequency simulation versus measured response, on a mount including a decoupler and inertia track (■, 0·1 mm P–P; △, 0·3 mm P–P; ——, 0·1 mm P–P simulated; ...., 0·3 mm P–P simulated).

response of the mount for different amplitudes. As seen in the figure, there is less than 5% error between simulated and measured response in the low-frequency range. The results indicate that the decoupler switching model and parameter identification techniques are valid under low-frequency large-amplitude excitations.

The high-frequency system model response for the simulation and experimental results at different amplitudes are shown in Figure 26. The agreement between the model and experimental results is significant and the model fits the measured data within 5% accuracy.

11. CONCLUDING REMARKS

In this paper, we provided a better understanding of the non-linear phenomena in a hydraulic mount. The non-linear model captured the desired response across the complete frequency and amplitude spectrum of interest. Insight into the decoupler switching parameters was documented. Continuous algebraic functions were developed to model the decoupler cage contact and its resulting effects on the mount response. Also, the decoupler leak flow was included in the model. The work conducted in this paper provides a reasonable understanding of the mount non-linear operation. A special experimental set-up was used to isolate the mount components for identifying their parameters. Using the identified parameters along with the non-linear model, we compared the model response with the mount measured data. In both low- and high-frequency comparisons, the model predicted the hydraulic mount behavior with less than 5% error. Small discrepancies between the results are attributed to experimental error in the measured parameters and general approximations made with the lumped parameter assumption. However, simulation results presented here are within acceptable levels by industry standards.

ACKNOWLEDGMENTS

The authors would like to acknowledge the financial support of the Natural Science and Engineering Research Council of Canada and the NVH Control System group at Cooper-Standard Automotive.

REFERENCES

1. R. M. BRACH and A. HADDOW 1993 *SAE Technical Paper Series* 931321. On the dynamic response of hydraulic engine mounts.
2. R. SINGH, G. KIM and V. RAVINDRA 1992 *Journal of Sound and Vibration* **158**, 219–243. Linear analysis of automotive hydo-mechanical mount with emphasis on decoupler characteristics.
3. W. FLOWER 1985 *SAE Technical Paper Series* 850975. Understanding hydraulic mounts for improved vehicle noise, vibration and ride qualities.
4. K. LEE and Y. CHOI 1995 *SAE Technical Paper Series* 951347. Performance analysis of hydraulic engine mount by using bond graph method.
5. G. KIM and R. SINGH 1993 *American Society of Mechanical Engineers, Journal of Dynamic System Measurement and Control* **115**, 482–487. Non-linear analysis of automotive hydraulic engine mounts.
6. G. KIM and R. SINGH 1995 *Journal of Sound and Vibration* **179**, 427–453. A study of passive and adaptive hydraulic engine mount systems with emphasis on non-linear characteristics.
7. G. KIM and R. SINGH 1992 *Transportation Systems, Proceedings of ASME/WAM DSC*, Vol. 44, 165–180. Resonance, isolation and shock control characteristics of automotive nonlinear hydraulic engine mounts.
8. G. KIM. 1992 *Ph.D. Thesis, Ohio State University*. Study of passive and adaptive hydraulic mounts.
9. M. F. GOLNARAGHI and R. NAKHAIE JAZAR 2000 *Journal of Vibration and Control* **V7**, 495–526. Development and analysis of a simplified nonlinear model of a hydraulic engine mount.
10. T. USHIJIMA, K. TAKANO and H. KOJIMA 1988 *SAE Technical Paper Series* 880073. High performance hydraulic mount for improving vehicle noise and vibration.

11. J. COLGATE, T. CHANG, C. CHIOU, K. LIU and M. KERR, 1995 *Journal of Sound and Vibration*, **184**, 503–528. Modelling of a hydraulic engine mount focusing on response to sinusoidal and composite excitations.
12. A. GEISBERGER A. 2000 *M.A.Sc. Thesis, University of Waterloo*. Hydraulic engine mount modelling, parameter identification and experimental validation.
13. L. F. SHAMPINE and M. REICHELT 1997 *Society for Industrial and Applied Mathematics* **18**, 1–22. The MATLAB ODE suite.
14. D. J. INMAN 1996 *Engineering Vibration*. Toronto, Ont.: Prentice-Hall.
15. S. GAU and J. COTTON 1995 *SAE Technical Paper Series* 951348. Experimental study and modelling of hydraulic mount and engine system.
16. J.-N. JUANG 1994 *Applied System Identification*. Toronto, Ont.: Prentice-Hall Canada Inc.
17. P. P. J. V. D. BOSH and A. V. DER KLAUW 1994 *Modeling, Identification and Simulation of Dynamical Systems*. Boca Raton, FL: CRC Press Inc.